RAPID COMMUNICATION

Accurate electron affinity of atomic rhodium and fine structure of its anion

Jiayi Chen(陈嘉逸)[1], Rui Zhang(张瑞)[1], Wenru Jie(揭文茹)[1], Qihan Liu(柳淇瀚)[1], and Chuangang Ning(宁传刚)[1,2,†]

[1] *Department of Physics, State Key Laboratory of Low-Dimensional Quantum Physics, Tsinghua University, Beijing* 100084, *China*
[2] *Frontier Science Center for Quantum Information, Tsinghua University, Beijing* 100084, *China*

(Received 3 February 2026; revised manuscript received 5 March 2026; accepted manuscript online 13 March 2026)

Rhodium (Rh) is a rare and expensive metal, mainly used as a catalyst. Investigating its electronic structure aids in elucidating the mechanisms that govern catalytic reactions. In this work, we employed the high-resolution slow-electron velocity-map imaging (SEVI) method to measure the electron affinity (EA) of Rh and the electronic structure of its atomic anion Rh^-. The EA of the Rh atom was determined to be 9216.8(4) cm^{-1} or 1.14273(5) eV, representing a fourfold enhancement in precision over the previous best result. Moreover, the energy levels of Rh^- were measured to be 0.41178(15) eV ($^3F_2$) and 0.28668(7) eV ($^3F_3$) above the ground state $^3F_4$, with an accuracy improved by factors of 110 and 50, respectively, compared to earlier measurements.

Keywords: electron affinity, fine structure, rhodium anion, slow-electron velocity-map imaging

PACS: 32.10.Hq, 32.10.Fn, 32.80.Gc, 37.10.Ty

DOI: 10.1088/1674-1056/ae5173 **CSTR:** 32038.14.CPB.ae5173

1. Introduction

Rhodium is a hard, silvery-white inert metal, notable for its rarity and high cost. It exhibits excellent mechanical strength, stable chemical properties, and good electrical conductivity. These characteristics render it suitable for manufacturing electrical contacts, electrodes, and high-temperature thermocouples, as well as for electroplating, where it provides a glossy, wear- and corrosion-resistant surface to materials like silver or platinum, thereby enhancing both aesthetics and durability.[1] Beyond these applications, rhodium and its compounds serve as highly efficient catalysts in organic synthesis processes,[2–4] in automotive exhaust purification,[5,6] and in hydrogen storage.[7,8]

These properties are intrinsically linked to rhodium's distinctive electronic structure. Its ground-state electron configuration is $4d^85s^1$, differing from its group counterparts Co($3d^74s^2$) and Ir($5d^76s^2$). This electronic configuration arises from the interplay of electron correlation effects, relativistic effects, and Hund's rules, leading to an electron rearrangement between the closely spaced 4d and 5s orbitals, in which one 5s electron occupies a 4d orbital. This unique electronic architecture profoundly determines rhodium's physical and chemical behavior. First, it renders rhodium chemically inert and highly corrosion-resistant. Second, it provides an ideal platform for catalysis: the nearly full d-orbitals can donate electron density into the antibonding π^* orbitals of reactant molecules (such as CO, NO, and olefins), thereby efficiently weakening and activating their chemical bonds.[9] Concurrently, rhodium possesses vacant valence orbitals capable of hybridizing and accepting electrons from reactants, facilitating the formation of key reaction intermediates. This dual capability — to donate and accept electrons — makes rhodium an essential active center in many important catalytic reactions.

A precise measurement of rhodium's electronic energy-level structure enables the quantitative description of its "electron-capturing ability", which, in turn, advances our understanding of its catalytic mechanisms and provides a theoretical foundation for designing next-generation, high-performance rhodium-based catalysts.

In contrast to its group counterparts cobalt (Co)[10] and iridium (Ir),[11] whose properties have been well established, research on the energy levels of rhodium anions was very limited before this work. To our knowledge, only two studies have been reported. In 1981, W. C. Lineberger's group used laser photodetachment electron spectrometry (LPES) to measure the electron affinity (EA) of Rh as 1.138(8) eV and determined the spin-orbit coupling splittings of the anion ground state ^3F to be 0.294(8) eV ($^3F_3$) and 0.418(8) eV ($^3F_2$) above the ground state $^3F_4$, respectively.[12] Later, in 1998, Scheer *et al.* measured Rh's EA using laser photodetachment threshold (LPT) spectroscopy and reported a refined electron affinity of 1142.89(20) meV.[13] Due to the unfilled d-orbitals in Rh^-, along with significant electron correlation and relativistic ef-

†Corresponding author. E-mail: ningcg@tsinghua.edu.cn

fects, theoretical calculations have been particularly challenging. As a result, accurate theoretical computational studies on this subject remain scarce.

In the present work, we report high-resolution photoelectron spectra of Rh^- obtained using the slow-electron velocity-map imaging (SEVI) method. The SEVI technique, characterized by both high resolution and the capability to simultaneously measure multiple transition channels, has contributed significantly to the measurement of EAs of atoms. For instance, high-precision EA values have been obtained via the SEVI method for main-group elements such as Ga,[14] As,[15] and Pb;[16] transition metals including Fe,[17] V,[18] Os,[19] and Y;[20] as well as for lanthanides and actinides such as La,[21] Ce,[22] U,[23] and Th.[24,25]

2. Experimental method

The experimental setup used in this work has been described in detail previously.[15,22,26–28] Only a brief overview is provided here. Rh^- ions were generated using a laser ablation ion source and subsequently trapped in an ion trap. The ion trap was mounted on a cryogenically cold head with an adjustable temperature in the range from 5 K to 300 K. The trapped ions were cooled via collisions with a buffer gas mixture (80% He and 20% H_2), which was delivered by a pulsed valve. After a controllable storage time of 5–45 ms, the trapped ions were ejected by applying pulsed voltages to the end-cap electrodes of the ion trap. After ejection, the ions were accelerated by a −1000 V high-voltage pulse in a Wiley–McLaren time-of-flight mass spectrometer and detected using a microchannel plate (MCP) detector.[29] The ion detector could be moved aside to allow a mass gate to select the ions of interest for the subsequent photoelectron energy spectroscopy. These ions were photodetached by a tunable dye laser (linearly polarized, 400–920 nm, linewidth 0.06 cm^{-1}). The wavelength of the dye laser was measured using a HighFinesse WS-600 wavelength meter with an accuracy of 0.02 cm^{-1}.

The photoelectrons were accelerated by the electric field in the imaging zone and were projected onto a microchannel-plate-enhanced phosphor screen. The hitting position of each photoelectron was recorded in real time by a charge-coupled device (CCD) camera in an event-counting mode.[30,31] The three-dimensional velocity distribution was reconstructed from the projected two-dimensional image using the maximum-entropy velocity-map Legendre inversion method.[32] Since the radius r of the photoelectron spherical shell is proportional to the electron velocity, the kinetic energy of the photoelectrons corresponding to different transition channels can be determined separately. This approach enables the measurement of both the energy levels of a negative ion and the corresponding neutral atom.

3. Results and discussion

3.1. Overview of the energy spectrum

Figure 1 shows the photoelectron energy spectra at a photon energy of 18020.98 cm^{-1} for an ion trapping time of 10 ms and an imaging voltage of 650 V. Given that the energy level structure of neutral Rh has been precisely measured,[12,33] the energy gaps between different peaks can assist in identifying the corresponding energy levels. Based on the preliminary data of the Rh^- fine structure, the known structure of the neutral species, and photodetachment selection rules, all observed peaks have been assigned. The corresponding transitions for the observed peaks are illustrated in Fig. 2, and Table 1 summarizes the assignment and binding energy for each peak. The photoelectron image in Fig. 1 and the spectral assignments in Fig. 2 indicate that the observed peaks originate predominantly from the p-wave detachment of an s-type electron. As a result, the signal intensity in laser photodetachment threshold (LPT) measurements is very low. This low intensity, governed by the Wigner threshold law, severely limits the accuracy and resolving power of the LPT method.[13,34]

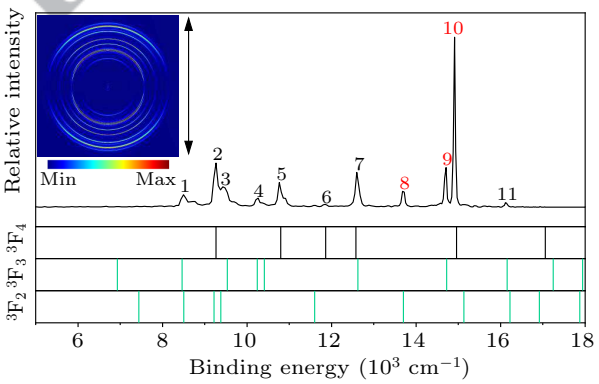

Fig. 1. Photoelectron energy spectra at photon energy $h\nu = 18020.98$ cm^{-1}. The vertical sticks below the spectra indicate the photodetachment channels from the anionic states labeled on the left to the specific neutral states, based on previously reported energy levels from literatures.[12,33] These sticks represent all possible transitions; some of them lack corresponding observed peaks, likely due to weak intensities. The black sticks represent transitions from the ground state $^3F_4$ of Rh^-, while the green sticks represent transitions from excited states $^3F_3$ and $^3F_2$ of Rh^-. Note: The peaks labeled in red were used for the precise determination of EA (peak 10) and fine structures (peaks 8 and 9).

Peak 2, located at approximately 9200 cm^{-1}, corresponds to the transition from the negative ion's ground state Rh^- $^3F_4$ to its neutral ground state Rh $^4F_{9/2}$. The binding energy of this channel defines the electron affinity of Rh, EA(Rh). However, if this photodetachment channel is directly selected for the EA measurement, an infrared laser is needed, which is outside the tuning range of our dye laser system. Instead, we chose the strong peak 10 to measure EA(Rh) as its final neutral state $^2F_{7/2}$ is well known with an accurate energy of 5690.97 cm^{-1} above the ground state of Rh.[33]

Based on the results obtained in this experiment, the related energy-level diagram is plotted in Fig. 2.

Table 1. Assignments of observed peaks and their binding energies. The expected binding energies are calculated values according to the present precise measurements and accurate energy levels of the neutral atom Rh.

Peaks	Levels($Rh^- \rightarrow Rh$)	Measured binding energy (cm^{-1})	Expected binding energy (cm^{-1})
1	$^3F_3 \rightarrow {}^4F_{7/2}/{}^3F_2 \rightarrow {}^4F_{5/2}$	8485(182)*	8434.5(5)/8493.6(11)
2	$^3F_4 \rightarrow {}^4F_{9/2}$ (EA)	9254(97)*	9216.7(4)
3	$^3F_3 \rightarrow {}^4F_{5/2}$	9443(215)*	9502.6(5)
4	$^3F_3 \rightarrow {}^2D_{5/2}$	10228(32)	10214.4(5)
5	$^3F_4 \rightarrow {}^4F_{7/2}$	10750(8)	10746.7(4)
6	$^3F_4 \rightarrow {}^4F_{5/2}$	11809(7)	11814.8(4)
7	$^3F_3 \rightarrow {}^2F_{7/2}$	12594.4(14)	12595.5(5)
8	$^3F_2 \rightarrow {}^2F_{5/2}$	13686.8(11)	13686.8(11)
9	$^3F_3 \rightarrow {}^2F_{5/2}$	14695.8(5)	14695.8(5)
10	$^3F_4 \rightarrow {}^2F_{7/2}$	14907.7(4)	14907.7(4)
11	$^3F_3 \rightarrow {}^4P_{5/2}$	16124.7(21)	16125.8(5)

*The uncertainties for these peaks were estimated from the full width at half maximum (FWHM) due to the distortion near the phosphor screen margin.

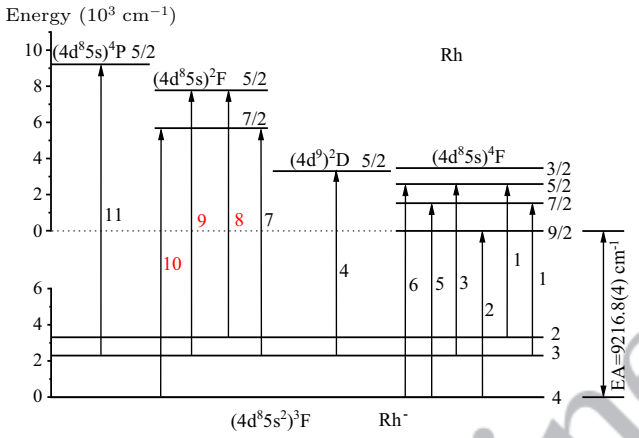

Fig. 2. Energy-level diagram related to the present measurement. Peak 10 (in red) is used for the EA measurement, and peaks 9 and 8 for the fine-structure measurement.

3.2. EA measurement

To accurately determine the binding energy for peak 10, measurements were conducted at a lower imaging voltage of 150 V because a lower imaging voltage yields a higher energy resolution, while a higher imaging voltage can cover a larger dynamic range of photoelectrons' velocities. SEVI can achieve an energy resolution of a few cm^{-1} near the photodetachment threshold. Therefore, we acquired spectra by varying the photon energy $h\nu$ from 14956 cm^{-1} to 15076 cm^{-1} in a step of 20 cm^{-1}. Figure 3 shows the photon energy $h\nu$ versus the squared radius r^2 of the photoelectron spherical shell. Linear fitting of $h\nu$ versus r^2 to the equation $h\nu = E_k + BE = \alpha \cdot r^2 + BE$ yields a binding energy $BE = 14907.7(4)$ cm^{-1} for the transition $^3F_4 \rightarrow {}^4F_{7/2}$, with uncertainties obtained from the fitting. Then, the electron affinity of Rh is determined as 9216.8(4) cm^{-1} or 1.14273(5) eV by subtracting the energy level of $^4F_{7/2}$ 5690.97 cm^{-1} from 14907.7(4) cm^{-1}.

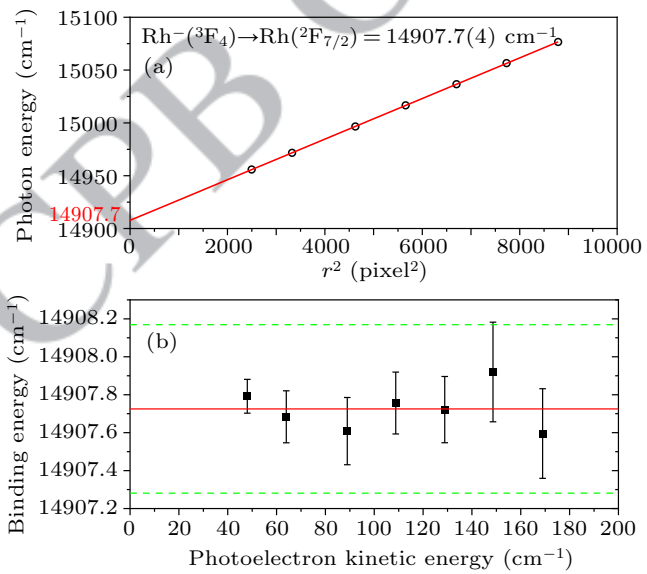

Fig. 3. (a) The squared radius r^2 for peak 10 versus the photon energy $h\nu$. A linear least-squares fit was performed using the formula $h\nu = BE + \alpha \cdot r^2$, where the vertical intercept 14907.7 cm^{-1} is the BE for peak 10. (b) Measured binding energy values of peak 10 plotted as a function of photoelectron kinetic energy. The dashed lines indicate an uncertainty of 0.4 cm^{-1}.

3.3. Fine structure measurement

SEVI has a higher energy resolution for photoelectrons with lower kinetic energy. Therefore, peaks 8 and 9 were selected to determine the binding energies of the fine-structure states $^3F_3$ and $^3F_2$ of Rh^-. To minimize the impact of the uncertainty of α on their BE measurement, a photon energy for measuring the BE of peak 8 or 9 was chosen such that its radius r was almost identical to the radius r_0 of peak 10 at a different photon energy. Under this condition, the formula is replaced by $E_k = E_{k0} + \alpha(r^2 - r_0^2)$ and $BE = h\nu - E_k$.[35] If r and r_0 are nearly identical, the uncertainty of BE is mainly contributed by the uncertainties of r and r_0, almost independent of the uncertainty of α. Compared with the general method $E_k = \alpha \cdot r^2$, this method can reduce the measurement error since both $h\nu$ and EA have been accurately measured.

Figure 4 illustrates the photoelectron intensity versus r^2 at two different photon energies, such that peaks 9 and 10 have almost the same radii.

Using this method, the binding energies of the fine-structure states were determined to be: $BE(^3F_3 \rightarrow {}^2F_{5/2}) = 14695.8(5)$ cm^{-1} and $BE(^3F_2 \rightarrow {}^2F_{5/2}) = 13686.8(11)$ cm^{-1}. As a result, the energy levels of $^3F_2$ and $^3F_3$ of Rh^- were determined to be 3321.2(12) cm^{-1} and

2312.2(6) cm^{-1} above the ground state ^{3}F$_4$, respectively. The measured results are in excellent agreement with those obtained from previous experiments, as shown in Table 2.

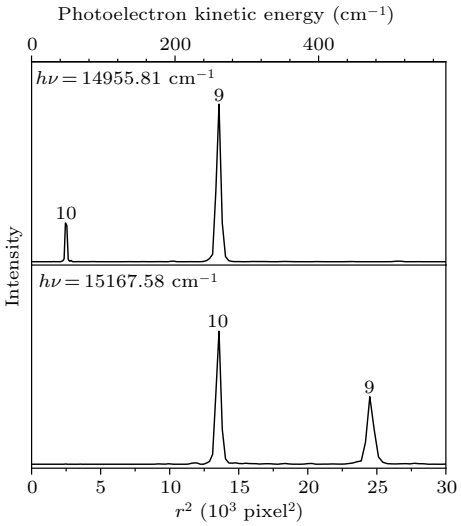

Fig. 4. Photoelectron energy spectra acquired at photon energies of 14955.81 cm^{-1} and 15167.58 cm^{-1}. Under these conditions, peak 9 in the top panel and peak 10 in the bottom panel have essentially the same kinetic energy.

Table 2. Electron affinity of Rh and fine structures of Rh$^-$ (eV).

Method	EA	Rh$^-$(^{3}F$_3$)–Rh$^-$(^{3}F$_4$)	Rh$^-$(^{3}F$_2$)–Rh$^-$(^{3}F$_4$)	Ref.
LPES	1.138(8)	0.294(8)	0.418(8)	[12]
LPT	1.14289(20)	/	/	[13]
SEVI	1.14273(5)	0.28668(7)	0.41178(15)	this work

4. Conclusions

In summary, we precisely measured the electron affinity of Rh and the fine structures of its negative ion using the slow electron velocity-map imaging (SEVI) method in combination with a cryogenically cold ion trap. The electron affinity of Rh was determined to be 9216.8(4) cm^{-1} or 1.14273(5) eV. The precision of the present work represents a fourfold improvement over previous studies. Furthermore, the energy levels of ^{3}F$_2$ and ^{3}F$_3$ of Rh$^-$ were determined to be 3321.2(12) cm^{-1} or 0.41178(15) eV, and 2312.2(6) cm^{-1} or 0.28668(7) eV above the ground state ^{3}F$_4$, respectively. The precisions were improved by factors of 110 and 50, respectively, compared to prior results.

Acknowledgements

Project supported by the National Natural Science Foundation of China (Grant Nos. 12374244 and 12341401).

The authors would like to thank Prof. Hongtao Liu for providing the Rh metal target.

References

[1] Livingstone S E 1975 *The Chemistry of Ruthenium, Rhodium, Palladium, Osmium, Iridium and Platinum* (Oxford: Pergamon) p. 1179
[2] Qi X T, Li Y Z, Bai R P and Lan Y 2017 *Acc. Chem. Res.* **50** 2799
[3] Shibata Y and Tanaka K 2012 *Synthesis* **44** 323
[4] Fagnou K and Lautens M 2003 *Chem. Rev.* **103** 169
[5] Dey S and Dhal G C 2020 *Polytechnica* **3** 26
[6] Shelef M and Graham G W 1994 *Catal. Rev.* **36** 433
[7] Azhar U, Iftikhar M T, Arif M, Rehman M A, Ibrahim T H and El-Kadri O M 2025 *Int. J. Hydrog. Energy* **101** 1448
[8] Li B, Ding Y, Kim D Y, Ahuja R, Zou G and Mao H K 2011 *Proc. Natl. Acad. Sci. USA* **108** 18618
[9] Lapointe S, Duari P and Gessner V H 2023 *Chem. Sci.* **14** 3816
[10] Chen X L and Ning C G 2016 *Phys. Rev. A* **93** 052508
[11] Lu Y Z, Zhao J, Tang R L, Fu X X and Ning C G 2020 *J. Chem. Phys.* **152** 034302
[12] Feigerle C S, Corderman R R, Bobashev S V and Lineberger W C 1981 *J. Chem. Phys.* **74** 1580
[13] Scheer M, Brodie C A, Bilodeau R C and Haugen H K 1998 *Phys. Rev. A* **58** 2051
[14] Tang R L, Fu X X, Lu Y Z and Ning C G 2020 *J. Chem. Phys.* **152** 114303
[15] Yan S T, Lu Y Z, Zhang R and Ning C G 2024 *Chin. J. Chem. Phys.* **37** 1
[16] Song C X, Yan S T, Godefroid M, Bieroń J, Jönsson P, Gaigalas G, Ekman J, Zhang X M, Chen C Y, Ning C G and Si R 2024 *J. Chem. Phys.* **160** 214307
[17] Chen X L, Luo Z H, Li J M and Ning C G 2016 *Sci. Rep.* **6** 24996
[18] Fu X X, Luo Z H, Chen X L, Li J M and Ning C G 2016 *J. Chem. Phys.* **145** 164307
[19] Lu Y Z, Zhang R, Song C X, Chen C Y, Si R and Ning C G 2023 *Chin. Phys. Lett.* **40** 093101
[20] Zhang R, Lu Y, Tang R and Ning C G 2023 *J. Chem. Phys.* **158** 084303
[21] Lu Y, Tang R, Fu X and Ning C G 2019 *Phys. Rev. A* **99** 062507
[22] Fu X X, Tang R L, Lu Y Z and Ning C G 2020 *Chin. Phys. B* **29** 073201
[23] Tang R L, Lu Y Z, Liu H T and Ning C G 2021 *Phys. Rev. A* **103** L050801
[24] Tang R L, Si R, Fei Z J, Fu X X, Lu Y Z, Brage T, Liu H, Chen C and Ning C 2021 *Phys. Rev. A* **103** 042817
[25] Zhang R, Lu Y Z, Yan S T and Ning C G 2025 *Phys. Rev. A* **111** 023102
[26] Tang R L, Fu X X and Ning C G 2018 *J. Chem. Phys.* **149** 134304
[27] Luo Z, Chen X, Li J and Ning C 2016 *Phys. Rev. A* **93** 020501
[28] Ning C G and Lu Y Z 2022 *J. Phys. Chem. Ref. Data* **51** 021502
[29] Wiley W C and McLaren I H 1955 *Rev. Sci. Instrum.* **26** 1150
[30] León I, Yang Z, Liu H T and Wang L S 2014 *Rev. Sci. Instrum.* **85** 083106
[31] Eppink A T J B and Parker D H 1997 *Rev. Sci. Instrum.* **68** 3477
[32] Dick B 2013 *Phys. Chem. Chem. Phys.* **16** 570
[33] Sansonetti J E and Martin W C 2005 *J. Phys. Chem. Ref. Data* **34** 1559
[34] Wigner E P 1948 *Phys. Rev.* **73** 1002
[35] Tang R L, Chen X L, Fu X X, Wang H and Ning C G 2018 *Phys. Rev. A* **98** 020501